Magnetosphere-ionosphere energy interchange in the electron diffuse aurora

G. V. Khazanov,[1] A. Glocer,[1] and E. W. Himwich[2,1]

[1]   The diffuse aurora has recently been shown to be a major contributor of energy flux into the Earth's ionosphere. Therefore, a comprehensive theoretical analysis is required to understand its role in energy redistribution in the coupled ionosphere-magnetosphere system. In previous theoretical descriptions of precipitated magnetospheric electrons ($E \sim 1$ keV), the major focus has been the ionization and excitation rates of the neutral atmosphere and the energy deposition rate to thermal ionospheric electrons. However, these precipitating electrons will also produce secondary electrons via impact ionization of the neutral atmosphere. This paper presents the solution of the Boltzman-Landau kinetic equation that uniformly describes the entire electron distribution function in the diffuse aurora, including the affiliated production of secondary electrons ($E < 600$ eV) and their ionosphere-magnetosphere coupling processes. In this article, we discuss for the first time how diffuse electron precipitation into the atmosphere and the associated secondary electron production participate in ionosphere-magnetosphere energy redistribution.

1.   Introduction

[2] In the theoretical description of precipitated magnetospheric electrons in regions of diffuse aurora, the major focus was always on the ionization and excitation rates of the neutral atmosphere, and/or heating of the thermal plasma [*Rees*, 1989]. A number of different approaches to the solution of the transport equation in the auroral ionosphere are presented in literature. Electron transport models for Earth's aurora have been developed by using a two-stream approach [*Banks et al.*, 1974], using a multistream approach that gives the details of pitch angle resolution [*Strickland et al.*, 1976] , using numerical implementation of the Boltzman-Landau kinetic equation [*Khazanov*, 1979], using a two-stream discrete ordinate method [*Stamnes*, 1981], applying a Feautrier solution [*Link*, 1992], using a discrete ordinate technique [*Lummerzheim and Lilensten*, 1994], and using a Monte Carlo technique [*Solomon*, 1993]. *Min et al.* [1993] took the discrete ordinate method of *Lummerzheim and Lilensten* [1994] to include small field-aligned ionospheric electric fields in order to study the influence of the ambipolar diffusion field on electron precipitation. *Peticolas and Lummerzheim* [2000] have developed a time-dependent electron transport model, which can simulate flickering aurora or fast moving auroral filaments.

[3] The global energy input into the atmosphere in the diffuse zone of the polar lights is substantially larger than the energy input associated with localized discrete auroral arcs. It turns out that the diffuse aurora, which is always present and widely distributed in rings around Earth's magnetic poles, collectively accounts for about three-quarters of the auroral energy precipitating into the ionosphere [e.g., *Newell et al.*, 2009]. The global pattern of electron precipitation can dramatically change the conductivity of the ionosphere, which can in turn influence the global pattern of magnetospheric convection, which are all affiliated with ionosphere-magnetosphere coupling processes [*Khazanov et al.*, 2003]. For this reason, diffuse auroral precipitation needs to be included in the development of global models for the Earth's magnetosphere.

[4] The diffuse aurora is characterized by a broad and fairly stable emission [*Lui and Anger*, 1973] and is thought to result from the precipitation of electrons that are not accelerated in the direction parallel to a magnetic field [e.g., *Winningham et al.*, 1975; *Lui et al.*, 1977; *Meng et al.*, 1979; *Fontaine and Blanc*, 1983; *Schumaker et al.*, 1989; *Johnstone et al.*, 1993].

[5] Diffuse precipitation of energetic electrons from the magnetosphere is a consequence of pitch angle scattering by plasma waves. In particular, it is expected that the diffuse aurora is caused by hot plasma sheet electrons that are pitch angle scattered into the loss cone by whistler mode waves near the equatorial plane [e.g., *Kennel and Petschek*, 1966; *Lyons*, 1974; *Johnstone et al.*, 1993]. These electrons are assumed to then precipitate into the atmosphere without further acceleration at high latitudes [e.g., *Winningham et al.*, 1975; *Lui et al.*, 1977; *Meng et al.*, 1979; *Fontaine and Blanc*, 1983; *Schumaker et al.*, 1989; *Johnstone et al.*,

---

[1]NASA GSFC, Greenbelt, Maryland, USA.
[2]Yale University, New Haven, Connecticut, USA.

Corresponding author: G. V. Khazanov, NASA/GSFC, Code 673, Greenbelt, MD 20771, USA. (george.v.khazanov@nasa.gov)

1993] and result a broad and fairly stable emission [*Lui and Anger*, 1973]. Diffuse auroral precipitation occurs over a broad range of geomagnetic latitudes that map along field lines from the inner magnetosphere and the plasma sheet, which is basically the region of closed magnetic field lines. Depending on the intensity of the geomagnetic storms, the magnetospheric electron precipitation can even reach magnetic latitudes $\sim 50°–55°$. The precipitation of energetic electrons in the diffuse auroral region is an important source of ionizing energy input to the middle atmosphere and heating of the thermal plasma. The strongest diffuse auroras are found on the postmidnight sector, while proton precipitation is important especially in the premidnight sector [*Nishimura et al.*, 2013]. The detailed morphology of the phenomena of precipitated magnetospheric electrons, as well as a comprehensive list of related studies, were presented by *Hardy et al.* [1987], and more recently by *Newell et al.* [2009, 2010].

[6] Secondary electrons (with energies below 500–600 eV) are produced by collisions of primary electrons of the diffuse aurora with the neutral atmosphere. The observational evidence for secondary electrons in the past has been discussed by *Frank and Ackerson* [1971], *Arnoldy et al.* [1974], and *Evans* [1974]; more recently, numerous Defense Meteorological Satellite Program (DMSP) observations related to various types of auroral events have been summarized by *Newell et al.* [2009, 2010]. These secondaries can escape back to the magnetosphere, can be trapped on closed magnetic field lines, and can deposit their energy back to the inner magnetosphere. As far as we know, there has been no prior study focusing on the aspect of diffuse auroral magnetosphere-ionosphere energy interchange that is affiliated with secondary electron production in this region and the escape of these secondary electrons back to the magnetosphere and conjugate ionosphere.

[7] Our study focuses on the magnetosphere-ionosphere energy interchange in the diffuse auroral region and is designed to answer the following question: How do diffuse auroral electron precipitation, with initial energies $E > 600$ eV, and the affiliated secondary electron population that it produces participate in ionosphere-magnetosphere energy and particle redistributions via different kinds of collisional processes with neutral and charged particles?

[8] This paper is organized as follows: The physical scenario of our simulations are discussed in section 2; the mathematical formalism and the numerical implementation of our superthermal electron model are briefly outlined in section 3; all results are presented in section 4; and finally, section 5 provides the summary and conclusions.

2. Physical Scenario

[9] The diffuse aurora occurs over a broad latitude range of $\phi = 55°–70°$ and is primarily caused by the precipitation of low-energy (0.5–30 keV) electrons originating in the central plasma sheet. A more precise and definitive relation between diffuse auroras and their particle source region was determined by simultaneous examination of the particle observations at geosynchronous orbit, the auroral display, and the auroral electron precipitation near its conjugate field line observed by the polar-orbiting DMSP 32 satellite and presented by *Meng et al.* [1979]. It was found that the spectral shape and differential fluxes of electrons

precipitated in diffuse auroras were very similar, and sometimes almost identical, to those of the trapped plasma sheet electrons located simultaneously in the conjugate magnetospheric equator. The characteristics of auroral electron precipitation are therefore determined by the particle features in the conjugate magnetospheric equator and the diffuse aurora is produced by the direct dumping of plasma sheet electrons. This similarity of characteristics shows indirect evidence for the absence of parallel electric fields in the region of electron diffuse aurora and it is expected that diffuse electron precipitation occurs simultaneously in both magnetically conjugate ionospheres.

[10] In terms of visual auroral morphology, the above identification implies that discrete auroras are produced by electrons from boundaries of the plasma sheet and diffuse auroras by electrons from the central plasma sheet, the earthward edge of the plasma sheet, and/or the outer radiation zone [*Ebihara et al.*, 2010]. The close relation between the diffuse aurora and plasma sheet electrons has been discussed [*Eather and Mende*, 1971; *Hoffman and Burch*, 1973; *Lui et al.*, 1977].

[11] Based on the discussion above, Figure 1 presents the physical scenario of our simulation of the energy exchanged between the magnetosphere and ionosphere during magnetospheric electron precipitation events into the two magnetically conjugate ionospheric regions including the affiliated production of secondary electrons ($E < 600$ eV), their escape back to the magnetosphere, their trapping on closed magnetic field lines, and their deposition of energy to thermal magnetospheric electrons.

[12] In Figure 1, we show this energy interchange on both the dayside and nightside of the space plasma. First, we illustrate the production of precipitating fluxes in the plasma sheet, shown as an orange cloud, where hot electrons, shown as tight orange spirals, are pitch angle scattered by whistler mode waves, shown in gray. The symmetrically precipitating primary electrons, entering into the conjugate northern and southern ionospheres, are shown by red arrows labeled Precipitating Primary Flux.

[13] The secondary electron flux ($E < 600$ eV) caused by this primary precipitation is shown by blue arrows labeled Escaping Secondary Flux. Blue spirals show the escaping particles that move along the magnetic field, some portion of which become trapped, illustrated by a blue cloud, and deposit energy to thermal electrons via Coulomb collisional processes. The conduction of this energy back to the ionosphere is shown by purple arrows labeled Returned Thermal Flux.

[14] The dayside of Figure 1 also shows, in yellow, the production of photoelectrons. These photoelectrons are produced in the same energy range as secondary electrons and are generated as a result of the interaction of Solar UV and X-ray radiation with the neutral atmosphere. In this paper, both secondary electrons and photoelectrons will be referred to as superthermal electrons (SE) and will be only distinguished below when we discuss the relative role of these populations in SE production on the dayside.

3. Theoretical Formalism

[15] Now, we consider the theoretical formalism of the physical scenario that we described above. The starting point
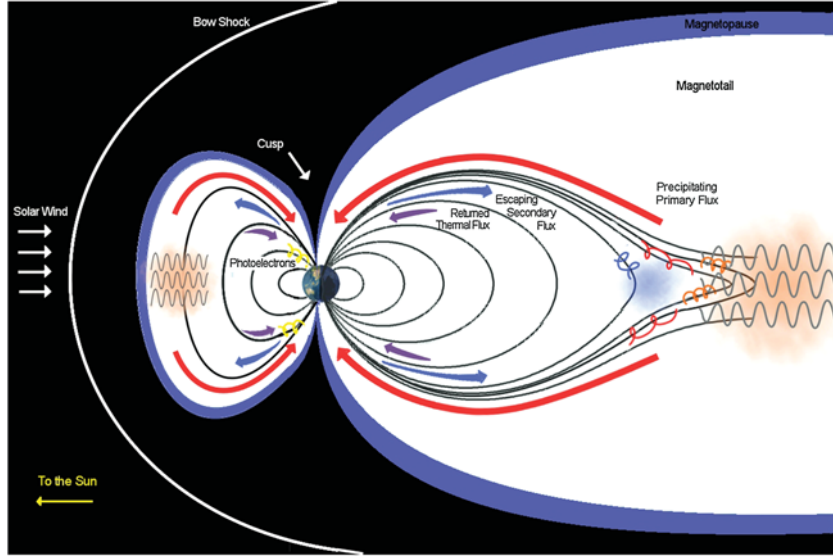
Figure 1. Illustration of I-M exchange processes: wave-particle interaction causes primary precipitation (red). Secondary electron fluxes can escape (blue) and precipitate into the conjugate region. Trapped particles deposit energy through collisions, which is thermally conducted (purple) back to the ionosphere. Photoelectrons (yellow) are shown on the dayside.

of our superthermal electron I-M coupling problem, for energies $E > 1$–2 eV, is the Boltzman-Landau kinetic equation that was derived and discussed by *Khazanov* [2011]. As we mentioned above, the dissipation process of magnetospheric electrons in the diffuse aurora is affiliated with the cascading of high-energy electrons toward small energies and the production of secondary, tertiary, and further such electrons. Such ionization cascade can be handled by just one single kinetic equation where all of the aforementioned processes are taken into account [*Khazanov et al.*, 1994]. Following *Khazanov* [2011], this equation can be written as

$$\frac{1}{v}\frac{\partial \Phi}{\partial t} + \mu\frac{\partial \Phi}{\partial s} - \frac{1-\mu^2}{2}\left(\frac{1}{B}\frac{\partial B}{\partial s} - \frac{F}{E}\right)\frac{\partial \Phi}{\partial \mu} + EF\mu\frac{\partial}{\partial E}\left(\frac{\Phi}{E}\right) = Q + \langle S \rangle \tag{1}$$

where $\Phi = 2Ef/m^2$ is the SE flux, $f = f(t, s, \mu, E)$ is the electron distribution function, v is SE velocity, t is time, s is the distance along the field line, E is the particle energy, and μ is the cosine of the pitch angle. The inhomogeneity of the geomagnetic field, B, is included, as well as other forces, such as electric fields, in F. Q is the SE source term and $\langle S \rangle$, which includes collision integrals, represents interactions with thermal electrons and ions, scattering with neutral particles and wave-particle interactions.

[16] This paper focuses only on the collisional processes in the diffuse electron aurora, and the electric field in kinetic equation (1) is expressed through the total gradient of the thermal electron pressure. The kinetic equation (1) is the gyroaveraged kinetic equation and the collisional terms in the bracket $\langle S \rangle$ represent such a type of the averaging procedure. In our paper we adopted the representation for all collisional processes in accordance with the book by *Khazanov* [2011, chapter 2, equation 2.5.2]. For the discussion related to this paper, the collisional terms in equation (1) can be presented as

[17] *Coulomb Collisions With Electrons and Ions*

$$\langle S_{ee} \rangle + \langle S_{ei} \rangle = An_e\left\{\frac{\partial}{\partial E}\left(\frac{\Phi}{E}\right) + \frac{1}{2E^2}\frac{\partial}{\partial \mu}\left[(1-\mu^2)\frac{\partial \Phi}{\partial \mu}\right]\right\} \tag{2}$$

where n_e is the density of the thermal electrons, $A = 2\pi e^4 lnL = 2.6 \times 10^{-12} \text{eV}^2\text{cm}^2$, and lnL is the Coulomb logarithm. The condition of plasma quasi-neutrality ($n_e = n_i$) has been used in arriving at (2).

[18] *Elastic Collisions With Neutral Particles*

$$\langle S_{ea} \rangle = n_\alpha \int I_\alpha(E, \chi)[\Phi(E, \mu') - \Phi(E, \mu)]\mathrm{d}\Omega \tag{3}$$

where the scattering ($\mu' \rightarrow \mu$) is described by the scattering angles (χ, η), with $\mu' = \cos\chi\cos\theta + \sin\theta\sin\chi\cos\eta$ (where θ is the electron pitch angle), and the solid angle $\mathrm{d}\Omega = \sin\chi\,\mathrm{d}\chi\,\mathrm{d}\eta$. The density of neutral particles of species α is n_α and the differential elastic cross section is $I_\alpha(E, \chi)d\Omega$.

[19] *Inelastic Collisions/Excitation*

$$\langle S_{ea}^* \rangle = n_\alpha \sum_j \left[\sigma_{\alpha j}^*(E + E_{\alpha j}^*)\Phi(E + E_{\alpha j}^*) - \sigma_{\alpha j}^*(E)\Phi(E)\right] \tag{4}$$

[20] *Inelastic Collisions/Ionization*

$$\langle S_{ea}^+ \rangle = n_\alpha \int\limits_{E+E_\alpha^+}^{2E+E_\alpha^+} I_\alpha^+(E', E' - E - E_\alpha^+)\Phi(E', \mu)\mathrm{d}E'$$
$$+ \frac{n_\alpha}{2\pi}\int\limits_{2E+E_\alpha^+}^{\infty} I_2^+(E', E)\int\limits_0^{2\pi}\Phi\left(E', \sqrt{(1-\mu^2)}\cos\eta\right)\mathrm{d}\eta\mathrm{d}E'$$
$$- n_\alpha\sigma_\alpha^+(E)\Phi(E, \mu) \tag{5}$$

where E_α^+ is the ionization energy, and $\sigma_{\alpha j}^*$ is the total cross section of scattering bringing a neutral particle into an

excited state characterized by a threshold energy $E^*_{\alpha j}$. We also have

$$\langle \sigma^+_{e\alpha} \rangle = \int\limits_0^{(E-E^+_\alpha)/2} I^+_\alpha(E, E_2) dE_2$$

which is the total cross section of ionization by an electron with energy E. $I^+_\alpha(E, E_2)$ is the appropriate differential cross section and E_2 is the energy of a secondary electron.

[21] In order to solve the kinetic equation (1) with collision terms presented by equations (2)–(5), we used a numerical method that has been discussed in detail in the book by *Khazanov* [2011, in Chapter 7]. This method is based on a solution to the kinetic equation along the entire length of a closed magnetic field line that is simultaneous for the two conjugate ionospheres and the magnetosphere. It allows the determination of the distribution in energy and pitch angle of superthermal electrons along the complete length of the field line, thereby avoiding the introduction of artificial boundaries between the ionosphere and magnetosphere and consequently avoiding problems introduced by the uncertainty of these boundary conditions. In addition, it automatically accounts for backscattered electrons in the atmosphere and plasmasphere, and avoids splitting SE into a loss cone and a trapped population. The method is not limited to specific situations, such as conjugated sunrise or symmetrical illumination of hemispheres, but is equally applicable to arbitrary illumination conditions, including the precipitation of electrons with magnetospheric origin, as presented in the scenario shown in Figure 1.

[22] Along a closed magnetic field line in the plasmasphere, the magnetic field is strongly inhomogeneous, while collisional diffusion terms are small due to the long mean free path. In order to decrease undesirable computational effects associated with approximation errors of the derivatives $\partial/\partial s$ and $\partial/\partial \mu$, it is convenient to change variables from (μ, s) to (μ_0, s), where

$$\mu_0 = \frac{\mu}{|\mu|} \sqrt{1 - \frac{B_0}{B(s)}(1 - \mu^2)} \qquad (6)$$

with B_0 and μ_0 denoting the magnetic field and the cosine of the pitch angle at the magnetic equator of the flux tube. This change of variables is desirable because $\Phi(\mu_0, s)$ now becomes a slowly varying function with s (without any external forces, μ_0 is simply the adiabatic invariant) that greatly reduces computational effects associated with approximation errors of the derivatives.

[23] The new variable μ_0 takes on values in the range $|\mu_{0B}| < |\mu_0| < 1$, where the lower boundary $\mu_{0B} = \sqrt{1 - B_0/B(s)}$ is a function of s. A specific feature of the algorithm used to solve the kinetic equation (1) in new variables (μ_0, s) is that the number of grid points in μ_0 varies with s because the definition interval varies with s. In the magnetosphere, where the inhomogeneity of the magnetic field causes μ_{0B} to vary significantly, the number of steps in μ_0 is increased by 2 for each step in s toward the magnetic equator. This scheme is illustrated in the book by *Khazanov* [2011, Figure 7.1] which shows the adopted grid as a function of s and $\theta_0 = \cos^{-1}\mu_0$. Since the magnetic field changes little in the ionosphere, while at the same time the step size in s is smaller in this region, the values μ_{0B} of adjacent altitude grid points would be undesirably close if this scheme was

extended all the way to the base of the ionosphere. Instead, we assume that the magnetic field is homogeneous below some altitude s_1 (typically 800 km) so that μ_{0B} is constant in the ionosphere.

[24] The number of grid points in the loss cone, $\mu_0 = \pm\sqrt{1 - B_0/B(s_1)}$, is constant for the complete field line. The trapping region is defined by $\sqrt{1 - B_0/B(s)} \leq |\mu_0| \leq \sqrt{1 - B_0/B(s_1)}$ and the loss-cone region by $\sqrt{1 - B_0/B(s_1)} \leq \mu_0 \leq 1$. The boundary conditions in s are imposed at conjugate points of the ionosphere, $-s_2$ and $+s_2$ at the altitude of 90 km or below (depending on the energy of the precipitated magnetospheric electrons) using the local approximation $(\partial/\partial s = 0)$.

[25] Using the numerical technique developed by *Khazanov et al.* [1993, 1994] the kinetic equation has been solved for these new variables $(t, E, \mu_0(\mu, s), s)$ under the following initial and boundary conditions:

$$\Phi(t = 0, s, \mu_0, E) = \Psi_0(s, \mu_0, E) \qquad (7)$$

$$\Phi(t, s = -s_1, \mu_0, E) = \Psi^-(t, \mu_0, E); -1 \leq \mu_0 \leq -\sqrt{1 - B_0/B(-s_1)}$$
$$\Phi(t, s = s_1, \mu_0, E) = \Psi^+(t, \mu_0, E); \sqrt{1 - B_0/B(s_1)} \leq \mu_0 \leq 1 \qquad (8)$$

$$\frac{\partial\Phi(\theta_0 = 0, \pi)}{\partial\theta_0} = 0; \theta_0 = \cos^{-1}\mu_0 \qquad (9)$$

$$\Phi^+(t, s, \mu_0 = \mu_{0_b}, E) = \Phi^-(t, s, \mu_0 = -\mu_{0_b}, E) \qquad (10)$$

$$\frac{\partial\Phi^+}{\partial\theta_0}(t, s, \mu_0 = \mu_{0_b}, E) = -\frac{\partial\Phi^-}{\partial\theta_0}(t, s, \mu_0 = -\mu_{0_b}, E) \qquad (11)$$

$$\Phi(t, s, \mu_0, E = 0; E = E_{max}) = 0 \qquad (12)$$

where Ψ_0 is the initial distribution in the flux tube; $\Psi\pm$ are the low altitude (in our case, 90 km) boundary fluxes which were calculated from equation (1) for the condition of local equilibrium; and θ_0 is the equatorial pitch angle. We have introduced the boundary conditions at intermediate altitude, 800 km, for the precipitated magnetospheric electron fluxes with the energies $E > 600$ eV with different initial energy spectra. For the purposes of this paper, we assume that the precipitated magnetospheric electrons are isotropic in pitch angle over the earthward direction and located at an initial height of 800 km. The energy distribution of these electrons is Gaussian [*Banks et al.*, 1974]

$$\Phi(E) = Ce^{-(E-E_0)^2/2\sigma^2} \qquad (13)$$

or Maxwellian [*Rees*, 1989]

$$\Phi(E) = CEe^{-E/E_0} \qquad (14)$$

where C is the normalization factor, E_0 is the characteristic energy of precipitated magnetospheric electrons, and $\sigma = 0.1E_0$ [*Banks et al.*, 1974]. The normalization factor C for equations (13) and (14) has been chosen to represent the energy flux of the precipitated magnetospheric electrons to the ionospheric region. Table 1 presents C values for Gaussian (equation (13)) and Maxwellian (equation(14)) spectra at the boundary of 800 km that are calculated for the

Table 1. Normalization Constant C for Different Spectra, Total Energy Flux 1 erg cm^{-2} s^{-1}

Mean Energy (keV)	0.4	0.8	1.0	2.0	3.0	5.0
Gaussian spectrum	1.14×10^{13}	1.25×10^{6}	7.94×10^{5}	1.98×10^{5}	8.82×10^{4}	3.17×10^{4}
Maxwellian spectrum	1.92×10^{3}	2.02×10^{2}	1.02×10^{2}	1.25×10^{1}	3.95×10^{0}	7.96×10^{-1}

total energy flux of 1 erg cm^{-2} s^{-1} for different mean energies, with an assumption that their pitch angle distribution is isotropic in the earthward direction. The Gaussian shape of the spectra is not very relevant to the precipitated electron flux in the diffuse aurora [*Mishin et al.*, 1990]. We only use such a form in one of the plots below for benchmarking purposes in order to emphasize the point of the paper.

[26] To perform the calculations, we used the following input for our SE model. For the purposes of this study, the Earth's magnetic field is assumed to be a dipole; however, the numerical algorithm that we developed could be used for any arbitrary magnetic field configuration, which will be demonstrated in follow up papers that will compare our model to particle observation results. Solar EUV and X-ray radiation spectra were obtained using the *Hinteregger et al.* [1981] model, while neutral thermospheric densities and temperatures were given by MSIS-90 [*Hedin*, 1991]. The electron profile in the ionosphere was calculated based on the IRI model [*Bilitza*, 1990] and extended in the plasmasphere region using the assumption that the electron thermal density distribution in the plasmasphere is proportional to the geomagnetic field as $n_e \sim B^2$. This case indicates some intermediate step occurring during plasmaspheric refilling [*Khazanov et al.*, 1984] and corresponds to the large L shells where electron diffuse aurora is taking place.

[27] Photoabsorption and photoionization cross sections for O, O_2, and N_2 were taken from *Fennelly and Torr* [1992]. Partial photoionization cross sections for O_2 and N_2 were obtained from *Conway* [1988], while partial photoionization cross sections of *Bell and Stafford* [1992] were adopted for atomic oxygen. Cross sections for elastic collisions, state-specific excitation, and ionization were taken from *Solomon et al.* [1988]. All of the calculations testing the effects of photoelectrons were performed for a local time of noon at equinox (midnight when not testing the effect of photoelectrons), with F10.7 and ⟨F10.7⟩ values of 150, chosen so the atmospheric conditions are symmetric and the solar radiation is at an average intensity level.

4. Results and Discussion

[28] We demonstrate our SE flux calculation in the electron diffuse auroral region for the conditions described above with an emphasis on the ionosphere-magnetosphere coupling processes. Specifically, we focus on the energy and particle flux redistribution between the magnetosphere and the two magnetically conjugate ionospheres. Our choice of a thermal density distribution in the plasmasphere $n_e \sim B^2$ at large L shells, $L \geq 5$, which is typical for the electron diffuse aurora, caused our flux calculations to be independent of L shell for $L \geq 5$, and all of our results are only presented for $L = 6$. The thermal density distribution choice of $n_e \sim B^2$ is very conservative and any effects shown by our calculation will be amplified for higher thermal densities.

[29] We first present our modeled SE omnidirectional fluxes at different altitudes in the northern ionosphere for the Gaussian (equation (13)) and Maxwellian (equation (14)) primary spectra, shown in Figure 2. These primary spectra correspond to the red precipitating arrows in Figure 1. In Figure 2, the Gaussian (Figure 2a) and Maxwellian (Figure 2b) primary beams are shown at the injection altitude of 800 km with black lines and have a total energy flux of 1 erg cm^{-2} s^{-1}, a mean distribution energy of 1 keV, and an energy range between 600 eV and 10 keV. Figures 2a and 2b also include the calculated secondary electron fluxes ($E < 600$ eV) for each of the primary spectra. These secondary fluxes, depicted as blue escaping fluxes in Figure 1, are presented at the altitudes of 150 km, 240 km, and 550 km in the northern ionosphere, below where the boundary condition for the primary spectra was imposed. The degradation of the primary beam with altitude is also included in the calculation and is visible in the results.

[30] For both the Gaussian (Figure 2a) and Maxwellian (Figure 2b) primary electron spectra, the secondary electron spectra show some distinctive characteristics at the altitudes of 150 km and 240 km. The trough between 2 and 3 eV comes from losses of secondary electrons that occur during the excitation of N_2 vibrational levels. This trough disappears at altitudes above 250–300 km, where Coulomb collisional processes will dominate over the collisional processes between the electrons and neutral particles.

[31] Figure 2c shows the ratio of secondary fluxes for a Gaussian distribution to a Maxwellian distribution. Even with the same total energy flux and mean energy E_0, the different shapes of the two primary electron spectra produce different intensities of secondary electrons. Again, it should be noted that a sharply shaped Gaussian (equation (13)) distribution is not typical in regions of electron diffuse aurora; such a distribution is presented above only as a benchmark to demonstrate the sensitivity of secondary electron spectra to the shape of the precipitating primary electron energy spectra. All other calculations presented below are based on a Maxwellian (equation (14)) distribution.

[32] Our next plot, Figure 3, illustrates the escaping SE flux with a color contour map of omnidirectional flux as a function of energy and distance along the magnetic field line. The fluxes are calculated for a Maxwellian primary beam with mean energy 0.4 keV and total precipitating energy flux of 1 erg cm^{-2} s^{-1}. The color contour displays how fluxes, shown from 0 to 500 eV, gradually decrease over the distance from the top of the ionosphere to the equatorial plane.

[33] Next, we illustrate the dependence of secondary ionospheric fluxes on the mean energy of the precipitating primary distribution. Figure 4 displays omnidirectional and directional SE fluxes in the northern ionosphere calculated for a Maxwellian primary spectrum with a constant energy flux of 2 erg cm^{-2} s^{-1} for all selected mean energies. Figures 4a and 4b include omnidirectional fluxes at 240 km and 550 km, respectively, for primary distribution
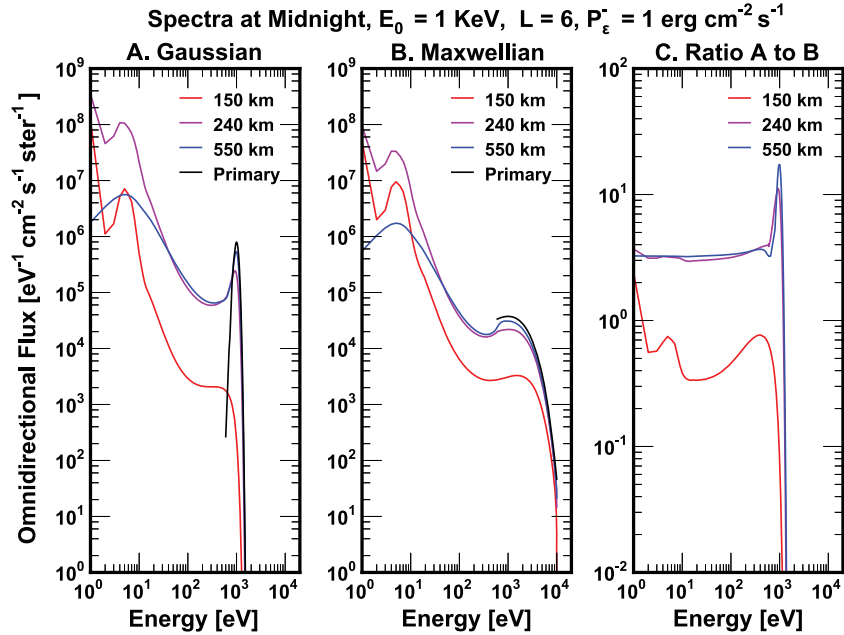
Figure 2. (a) Omnidirectional modeled fluxes with all processes included at altitudes of 150 km (red), 240 km (purple), and 550 km (blue) in the northern ionosphere for a Gaussian primary spectrum at the injection altitude of 800 km (black). (b) Omnidirectional fluxes for a Maxwellian primary spectrum. (c) Ratio of secondary fluxes produced by a Gaussian-to-Maxwellian distribution. All primary spectra distributions have a total precipitating energy flux of 1 erg cm^{-2} s^{-1} and mean distribution energy of 1 keV.

mean energies ranging from 0.4 keV (shown in red) to 5.0 keV (yellow). With the total precipitating energy flux held constant, as the mean energy of the particles in the Maxwellian primary distribution increases, there are fewer particles needed to carry the same total energy. As a result, and the peak of the distribution flattens in the energy range of the primary beam ($E > 600$ eV).
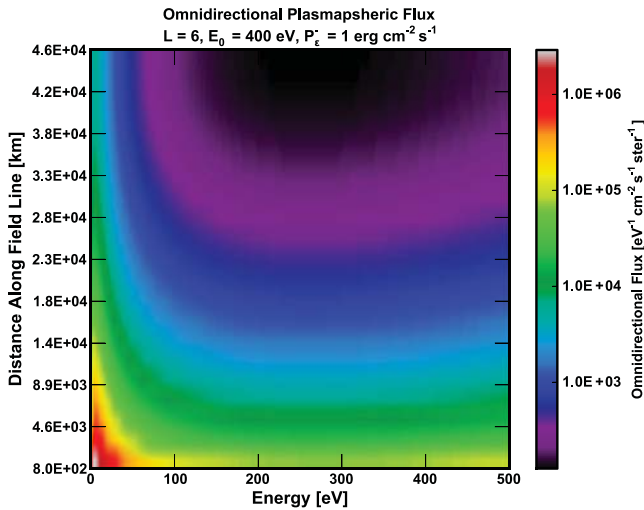
Figure 3. Omnidirectional flux in the plasmasphere (E 1–500 eV) beginning in the northern ionosphere at altitudes of 800 km to 46,000 km along the field line, calculated for symmetric Maxwellian primary precipitation with a mean distribution energy of 0.4 keV and a total precipitating downward flux of 1 erg cm^{-2} s^{-1}.

[34] In Figure 4, the omnidirectional secondary fluxes ($E < 600$ eV) at 240 km (a) and 550 km (b) maintain the same structure at each different mean energy. However, as the mean energy of the primary distribution increases, the secondary fluxes also decrease in intensity by more than an order of magnitude. This decrease is due to two processes: the decreased efficiency of secondary electron production at higher mean energies, and the increased ionospheric penetration depth of higher-energy particles, which makes the resultant secondary electrons less likely to escape upward from the ionospheric altitudes where their mean free path becomes less than the scale height of the neutral atmosphere.

[35] Figure 4c includes directional fluxes down (solid lines) and up (dashed lines) at 550 km in the northern ionosphere for three mean energies of the Maxwellian primary distribution: 0.4 keV (red), 1.0 keV (green), and 3.0 keV (light blue). In the energy range of the primary beam ($E > 600$ eV), fluxes down are greater than fluxes up due to the degradation of the precipitating beam in the ionosphere. However, the secondary electron flux ($E < 600$ eV) escaping up out of the northern ionosphere is greater than the flux precipitating into the ionosphere in this energy range. As described above, we include symmetric precipitation in the two conjugate ionospheres. In Figure 4c, we display directional fluxes for the northern ionosphere, where the precipitating secondary fluxes include a contribution from the particles escaping the northern ionosphere that are backscattered from the plasmasphere, as well as a contribution from the secondary fluxes returned from the conjugate southern ionosphere. These downward secondary fluxes in the northern ionosphere have undergone low-energy degradation due to trapping and scattering processes during their travel through the plasmasphere. Consequently, they have a lower
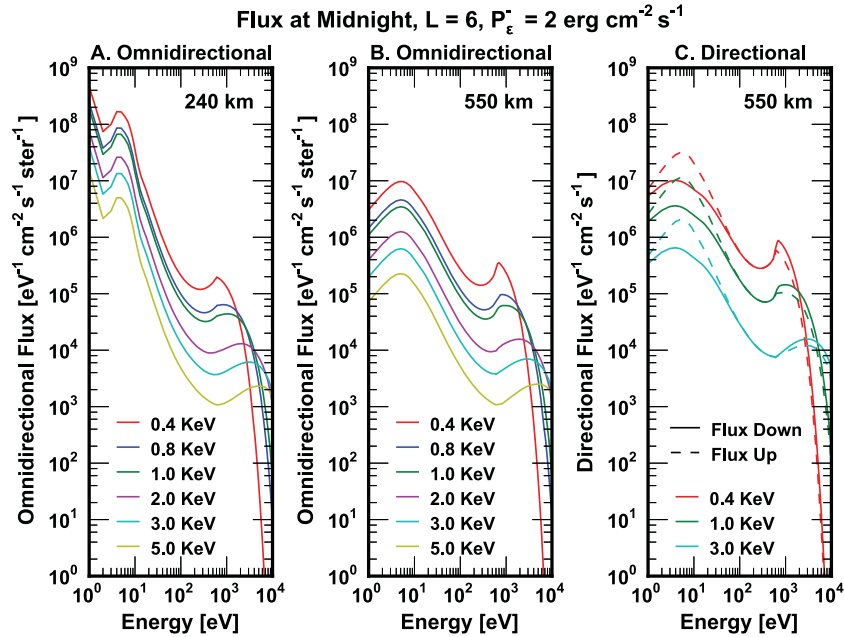
Figure 4. (a) Omnidirectional modeled fluxes with all processes included at the altitude of 240 km in the northern ionosphere for six different Maxwellian primary distribution mean energies. (b) Omnidirectional fluxes for the same Maxwellian mean energies at 550 km. (c) Directional fluxes down (solid lines) and up (dashed lines) at 550 km for Maxwellian mean energies 0.4 keV (red), 1.0 keV (green), and 3.0 keV (light blue). All fluxes calculated for a Maxwellian primary spectra distribution with a total precipitating energy flux 2 erg cm^{-2} s^{-1}.

intensity than the secondary fluxes escaping the northern ionosphere which result directly from the primary precipitation in this ionosphere. This effect directly illustrates the interaction of the two ionospheres and the magnetosphere as a connected system.

[36] Figure 5 demonstrates the modeled effect of various processes on the magnitude of omnidirectional fluxes in the northern ionosphere. SE fluxes at 550 km for different limited cases are shown and are calculated for a Maxwellian primary spectrum with total energy flux 3 erg cm^{-2} s^{-1} and mean energy 1 keV. The case when all processes—including secondary production, cascading, and reflection in both ionospheres—are modeled, is shown in red. In blue, this same case is shown with secondary production removed from the calculation in the two conjugate ionospheres, illustrating the significant difference between the number of low-energy electrons ($E < 600$ eV) produced using our model and models that omit secondary production.
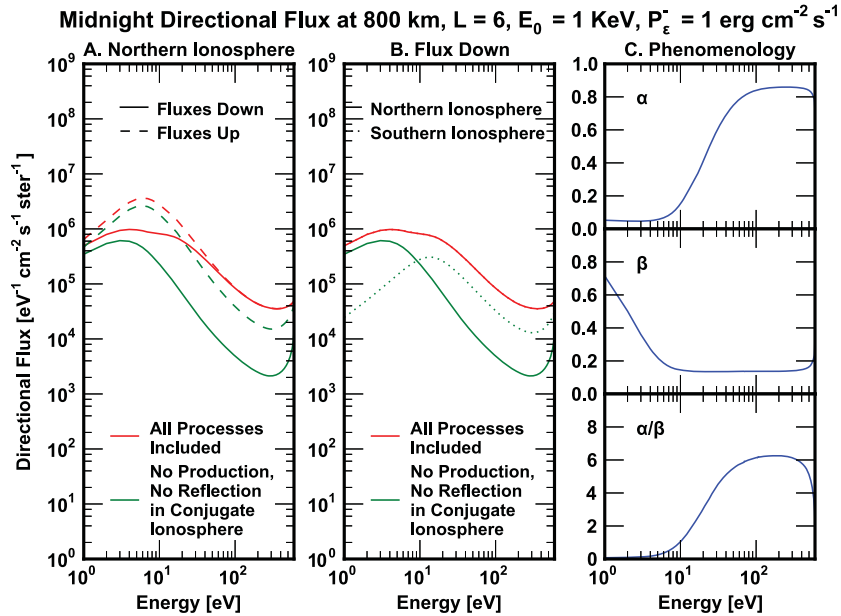
[37] The green line in Figure 5 shows a case with all processes included in the northern ionosphere, but with the processes of primary precipitation, secondary production, and reflection entirely removed from the southern ionosphere. In this case, flux in the northern ionosphere decreases because it has lost its contribution from transient secondary fluxes that escape the southern ionosphere and travel through the magnetosphere to precipitate in the northern ionosphere.

[38] Finally, the yellow line demonstrates the modeled effect of the presence of an ionospheric potential barrier above 800 km, which causes fluxes escaping from the ionosphere to be entirely reflected back down, making the precipitating and escaping fluxes in the northern ionosphere exactly the same. In this case, precipitating flux no longer

includes a degraded transient portion from the southern ionosphere and matches the higher escaping flux seen in Figure 3c; this causes omnidirectional secondary fluxes to
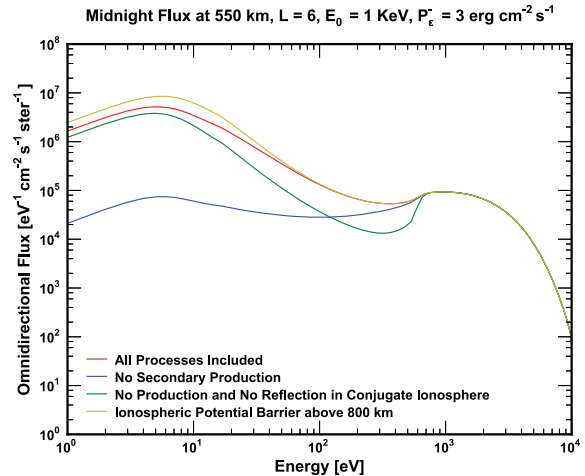
Figure 5. Omnidirectional modeled fluxes at 550 km in the northern ionosphere calculated for a Maxwellian primary spectrum with total precipitating energy flux 3 erg cm^{-2} s^{-1} and mean distribution energy 1 keV for four different cases: all processes of primary precipitation, secondary production, and reflection included in both ionospheres (red); no secondary production in either ionosphere (blue); all processes in the northern ionosphere but no reflection, secondary production, or reflection in the southern ionosphere (green); and the presence of a magnetic potential barrier at 800 km in the northern ionosphere (yellow).

Midnight Directional Flux at 800 km, L = 6, E_0 = 1 KeV, P_{ε}^{-} = 1 erg cm^{-2} s^{-1}

Figure 6. Directional modeled secondary fluxes ($E < 600$ eV) at 800 km using a Maxwellian primary spectrum with mean energy 1 keV and total precipitating energy flux 1 erg cm^{-2} s^{-1} for two cases: all processes of primary precipitation, secondary production, and reflection in both ionospheres (red), and all processes in the northern ionosphere but none in the southern conjugate ionosphere (green). (a) Directional fluxes up (dashed lines) and down (solid lines) in the northern ionosphere for the two cases. (b) Downward fluxes alone in both the northern (solid lines) and southern (dotted lines) ionospheres for the two cases.

increase and doubles the energy deposition of SE fluxes in the heating rate of the thermal electrons.

[39] A more detailed comparison of the limited case with processes removed in the southern ionosphere is shown in Figure 6. The figure compares the case with all processes included and the case with no production and no reflection in the conjugate ionosphere; these are shown in red and green, respectively, to correspond with Figure 5. Again, for this limited case, primary precipitation, secondary production, and backscattering have been removed from the southern ionosphere. In this figure, we present fluxes only for secondary production ($E < 600$ eV) because, due to the boundary condition of primary precipitation, the high-energy directional fluxes behave identically to those in Figure 4c.

[40] Figure 6a displays the directional fluxes down (solid lines) and up (dashed lines) at the boundary of the northern ionosphere, an altitude of 800 km, for the two different cases. For the case with all processes included (red), the secondary directional fluxes behave identically to Figure 4c: The precipitating secondary fluxes down have partially degraded because of the contribution from fluxes that travel through the plasmasphere after escaping the conjugate region, while the fluxes up in the northern ionosphere are a direct product of primary precipitation into this ionosphere. In the case with no fluxes returned from the conjugate region (green), the fluxes down in the northern ionosphere have a lower intensity, and a different structure, than the downward fluxes with all processes included (red), because they lack any contribution from transient flux escaping from the southern ionosphere.

[41] Even when this transient portion of incoming fluxes is completely removed, there is still a significant incoming flux (solid green line) generated by the return of trapped particles in the magnetosphere to the source ionosphere due to electron scattering into the loss cone. Clearly, because these downward secondary fluxes in the northern ionosphere are lower than those downward fluxes with all processes included (solid red line), the escaping secondary fluxes in the case of no reflection (dashed green lines) will also have consistently lower intensity than the escaping fluxes in the case with all processes included (dashed red lines).

[42] Figure 6b illustrates the interplay of the two conjugate ionospheres, northern (solid lines) and southern (dotted lines), during these two cases by comparing the downward fluxes at the boundary of each ionosphere. In the case with all processes included (red), precipitation occurs symmetrically in both the northern and southern ionospheres; the downward flux is identical and only one line (solid red line) is presented. However, in the case of no reflection (green), where primary precipitation, secondary production, and reflection are removed from the southern ionosphere, there are no upward fluxes at the boundary of the southern ionosphere and the downward fluxes at the boundary of the northern (solid green line) and southern ionosphere (dotted green line) are very different. The downward fluxes in the southern ionosphere are greater than those in the northern ionosphere, except for very low energies ($E < 10$ eV). Such behavior is not very obvious; because the contribution of transient secondary flux from the conjugate region is present in the southern ionosphere but not in the northern ionosphere, it might be expected that fluxes precipitating into the
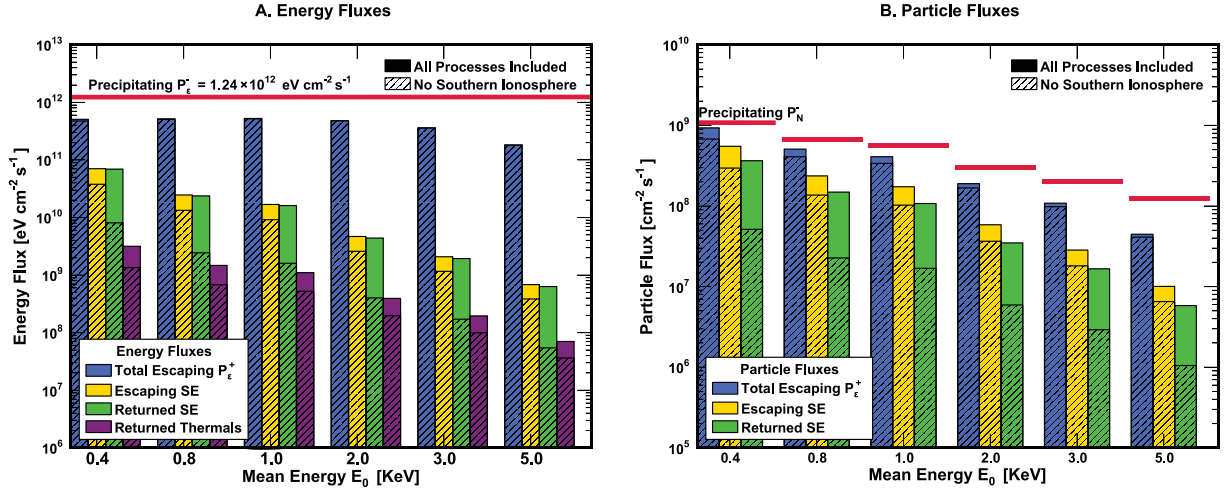
Figure 7. Histograms with integrated directional energy (particle) fluxes at the boundary of the northern ionosphere calculated for different mean energies using a Maxwellian primary distribution with total precipitating energy flux 2 erg cm^{-2} s^{-1}. At each mean energy we display: precipitating primary energy (particle) flux (red), total escaping energy (particle) flux (blue), escaping SE energy (particle) flux, $E <$ 600 eV (yellow), and total returned/precipitating SE energy (particle) flux, $E <$ 600 eV (green). (a) The energy flux histogram also includes thermal flux returned to the ionosphere in purple. These quantities are shown both for the cases of all processes of primary precipitation, secondary production, and reflection included in both ionospheres (solid bars) and with all processes included in the northern ionosphere but all removed in the southern (dashed bars).

southern ionosphere are greater than those precipitating into the northern ionosphere over all energies.

[43] However, we were able to understand this behavior by referring to the phenomenological model of the ionosphere-plasmasphere system developed by *Khazanov* [2011] and *Khazanov et al.* [2013]. Adopting a notation in accordance with *Khazanov et al.* [2013, Figure 2], the fluxes into the northern ionosphere F_1^- can be given by

$$F_1^- = \alpha F_2^- + \beta F_1^+ \qquad (15)$$

and fluxes into the southern ionosphere F_2^+ given by

$$F_2^+ = \alpha F_1^+ + \beta F_2^- \qquad (16)$$

where F_2^- is flux escaping the southern ionosphere, F_1^+ is flux escaping the northern ionosphere, β is the part of SE energy returned from the plasmasphere to the source ionosphere due to electron scattering in the loss cone, and α is the pure part of plasmaspheric transparency, the particles not lost or scattered. Because we have that $F_2^- = 0$ for our limited case with the southern ionosphere removed, these fluxes are equivalent to $F_1^- = \beta F_1^+$ and $F_2^+ = \alpha F_1^+$, respectively, implying that

$$\frac{F_2^+}{F_1^-} = \frac{\alpha}{\beta} \qquad (17)$$

[44] The parameters alpha and beta, which are calculated, based on the full kinetic solution, according to the phenomenological model by Khazanov et al., are displayed along with their ratio in Figure 5c. The parameter α, the transparency of particles not lost or scattered as they pass between two conjugate ionospheres, approaches one for particles with higher energies, which are more likely to avoid collision due to the decrease in the Coulomb cross section

with energy. The parameter β, the fraction of particles that return to the initial ionosphere after being scattered in the plasmasphere, has the same energy dependence as the Coulomb cross section. While the ratio α/β is constant for energies with $E > 10$ eV, it decreases to below one for energies less than $\sim$10 eV. This trend is seen exactly in the fluxes of F_2^+, flux down into the southern ionosphere (solid line) and F_1^-, flux down into the northern ionosphere (dashed line), shown in Figure 6b, which are equal at $\sim$ 10 eV, where the ratio α/β equals one.

[45] Taken together, Figures 5 and 6 clearly demonstrate the effect of the removal or inclusion of different processes on the energy and particle fluxes in the two ionospheres, which are each dependent on the flux in the conjugate ionosphere and on plasmaspheric SE transport. We continue and expand on this discussion of the interplay between the two conjugate ionospheres and the magnetosphere by presenting, in Figure 7, the total (integrated) directional energy and particle fluxes in the northern ionosphere. To reemphasize the mutual dependence of the conjugate ionospheres and plasmasphere, we include integrated fluxes for symmetric conditions of primary precipitation, reflection, and secondary production in each ionosphere, as well as for asymmetric conditions, in which primary precipitation, secondary production, and reflection are removed from the southern ionosphere.

[46] Figure 7 includes different integrated energy and particle fluxes in the northern ionosphere over a range of mean energies. The figure presents histograms of integrated (Figure 7a) energy and (Figure 7b) particle fluxes, on the left and right, respectively (note the difference in scale and units on the dependent axis). In each histogram, the fluxes are calculated at the boundary altitude of 800 km, for a Maxwellian primary spectrum with total energy flux 2 erg cm^{-2} s^{-1},

equivalent to 1.24×10^{12} eV/cm^2 s, shown as a red line in Figure 7a. Along the independent axis, both the integrated energy and particle flux histograms display fluxes calculated for a range of mean energies from 0.4 keV to 5.0 keV. While downward precipitating energy flux is constant across all mean energies, as shown by the red horizontal line in Figure 7a, this constant energy flux causes the precipitating particle flux to vary inversely as a function of mean energy, as shown by the staggered red horizontal lines representing downward particle flux.

[47] Each histogram displays the integrated energy (Figure 7a) or particle (Figure 7b) flux of three quantities: all electrons escaping the ionosphere (blue, integrated over 1 eV–10 keV), escaping SE electrons (yellow, integrated over 1–600 eV), and SE electrons returned to the ionosphere (green, integrated over 1–600 eV). The solid colors in both histograms represent the magnitude of fluxes when all processes, including secondary production, reflection from the conjugate ionosphere, and cascading, are modeled. The dashed lines represent the results when all these processes are removed in the conjugate ionosphere.

[48] In the case with all processes included (solid colors), over mean energies 0.4 keV to 5.0 keV, the total energy that escapes the ionosphere (Figure 7a, blue) as a percent of precipitating energy (red) decreases from 40% to 15%. Similarly, the number of total particles that escape (Figure 7b, blue) as a percent of precipitating particles (red) decreases from 85% to 35%. Simultaneously, the escaping SE particles (Figure 7b, yellow) as a percent of total escaping particle flux (Figure 7b, blue) decreases from 55% to 20%. This decrease in escaping flux with the increasing mean energy of the primary beam was also observed in Figures 4a and 4b. As discussed above, it is due to two processes: the decreased efficiency of the secondary electron production at higher mean energies and the increased ionospheric penetration depth of high-energy particles, which makes their resultant secondary electrons less likely to escape upward from the ionospheric altitudes where their mean free path becomes less than the height scale of the neutral atmosphere.

[49] Each histogram also includes these values for the case when the conjugate ionosphere is removed completely (shown in dashed lines) and no primary beam, secondary production, nor reflection occurs in the southern ionosphere. This case corresponds to the case shown in green on Figures 5 and 6. These fluxes are significantly lower than the fluxes with all processes included, as explained above in the description of Figure 6a. For each mean energy, there is a relatively larger difference between the returned SE (green) and the escaping SE (yellow) energy and particle fluxes when the conjugate ionosphere is removed (dashed lines) than when all processes are included, also noted previously in the description of Figure 6a.

[50] The energy flux histogram (Figure 7a) also includes the conductivity flux of the thermal electrons (purple), which is defined by the following two-step integration process. First, we calculate the local heating rate along the selected magnetic field line, as defined by *Khazanov* [1979]:

$$Q = A n_e \left\{ \phi_0(E_{\min}) + \int_{E_{\min}}^{\infty} \frac{\phi_0(E)}{E} dE \right\} \qquad (18)$$
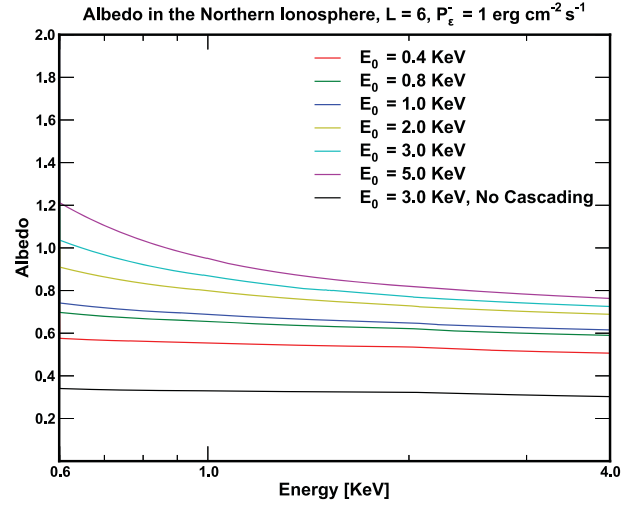
Figure 8. Albedo, the ratio of fluxes escaping the northern ionosphere to fluxes precipitating into the northern ionosphere, presented for different mean energies from 0.4 keV (red) to 5.0 keV (purple). Fluxes are calculated for a Maxwellian primary distribution with constant downward precipitating flux of 1 erg cm^{-2} s^{-1}. The black line shows albedo when cascading processes are removed in the northern ionosphere for a mean energy of 3.0 keV.

where $\phi_0(E_{\min})$ is omnidirectional flux at the energy of 1 eV, the lowest energy of our simulation. Because thermal conductivity is the fastest process of energy loss in the plasmasphere, all energy that collects along the field tube will flow down with the energy flux at the ionospheric boundary calculated as

$$P_i = \int_{s_0}^{s_i} Q \frac{B_i}{B} ds \qquad (19)$$

where the i subscript indicates quantities at the ionospheric boundary and the 0 subscript is for the equatorial plane. The integral only covers half of the flux tube because the energy deposition is shared between the two conjugate foot points of the field line.

[51] This energy deposition, labeled as Returned Thermals (purple) in the histogram, range from 3×10^9 eV/cm^2 s to 7×10^7 eV/cm^2 s. This returning flux is only 7%–12% of the escaping SE energy flux; the missing energy must have been trapped in the plasmasphere.

[52] While the histograms of Figure 7 are useful to compare integrated quantities, they hide changes that occur as a function of particle energy. Though we compare the ratio of the number of particles escaping to the number particles precipitating in one ionosphere in Figure 7b, we would also like to discuss the change in this ratio over the energy range of primary fluxes, 600 eV–10 keV.

[53] Following *Khazanov* [2011] and *Khazanov et al.* [2013], we define albedo as

$$A = F_1^+ / F_1^- \qquad (20)$$

where F_1^+ is flux escaping the northern ionosphere and F_1^- is flux precipitating into the northern ionosphere.

[54] Figure 8 displays this ratio for different mean energies from 0.4 keV (red) to 5.0 keV (purple), calculated for a
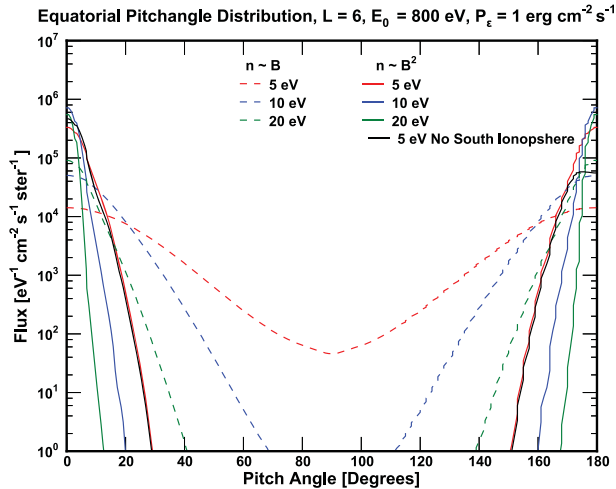
Figure 9. Equatorial distribution of flux over pitch angles from 0°–90° (leaving the northern ionosphere) and 90°–180° (leaving the southern ionosphere) for thermal densities of n ~ B (dashed lines) and n ~ B^2 (solid lines), shown for symmetrically precipitating particles with energies of 5 eV (red), 10 eV (blue), and 20 eV (green). Particles with energies of 5 eV are compared with the case of precipitation removed in the southern ionosphere (black line). Fluxes are calculated using a Maxwellian primary distribution with total precipitating energy flux 1 erg cm^{-2} s^{-1} and mean energy 0.8 KeV.

Maxwellian primary distribution with constant precipitating downward flux of 1 erg cm^{-2} s^{-1}. As seen from this figure, the albedo increases with decreasing energy. This is because cascading from higher energies becomes increasingly important with decreasing energy for the reflected flux, while the precipitating flux is not changing at all energies as it was imposed by boundary conditions at an altitude of 800 km. Also, albedo increases over all energies in the range 600 eV–10 keV as mean energy increases, and below ~1 keV albedo increases for all mean energies, with higher mean energies having a steeper increase. This increase is due to cascading processes; as the mean energy of the primary distribution increases, more particles have higher energies and cause further cascading through lower energies. Indeed, when cascading processes are removed in the northern ionosphere (shown for $E_0 = 3.0$ keV in black), albedo decreases and does not display any increase for $E < 1$ keV.

[55] Next, we illustrate the differences in the equatorial pitch angle distribution of fluxes based on electron density dependence in the plasmasphere, presented in Figure 9. This figure includes equatorial pitch angle distribution from 1°–180°, with 0°–90° leaving the northern ionosphere, and 90°–180° leaving the southern ionosphere, modeled using a Maxwellian primary distribution spectrum with mean energy 0.8 keV and total energy flux 1 erg cm^{-2} s^{-1}. As described above, we model identical symmetric primary precipitation in both ionospheres, which gives the equatorial pitch angle distribution symmetry across 90°. However, we also present one case of nonsymmetric precipitation, the limited case with no precipitation and no reflection in the southern ionosphere; in this case, shown in black, pitch angle distribution is also asymmetric.

[56] Figure 9 includes two different thermal electron plasmaspheric densities, $n_e \sim B$ (dashed lines), and $n_e \sim B^2$ (solid lines). With $n_e \sim B$, there is greater thermal density and therefore greater pitch angle scattering and a range of pitch angles more evenly distributed away from the loss cone than with $n_e \sim B^2$, which is a more realistic case during the refilling of a depleted flux tube at the large L shell of $L = 6$. For each density, fluxes for three energies are presented: 5 eV (red), 10 eV (blue), and 20 eV (green). In Figure 9, electrons with the energy 5 eV have lowest fluxes at 0 degrees and 180 degrees because as the energy of particles decreases, they are more likely to be pushed into the trapped zone, and will have lower intensity in the loss cone.

[57] It is also interesting to point out the behavior of the trapped SE population in comparison between symmetric and nonsymmetric precipitation cases that is only displayed in Figure 9 for the 5 eV electrons. The red and the black lines corresponding to these two cases almost follow each other all the way to the loss cone boundary. The similarity of the pitch angle distribution between the two cases in the trapped zone improves with increasing energy (not shown here). As a result, treatment of SEs with a bounce-averaged version of equation (1) (formalism derived and presented by *Khazanov* [2011]) may be appropriate. Such an approach would greatly simplify the calculation of the SEs on a global scale.

[58] In all of the results described above, we have only dealt with primary precipitated fluxes at midnight, as pictured on the right-hand side of Figure 1. However, as shown by data [see *Hardy et al.*, 1987], dayside precipitation also takes place. In this case, the SE population has an additional source: photoelectrons, as pictured in yellow on the left-hand side of Figure 1. Additionally, photoelectrons can generate secondary electrons from their collisions with neutral particles in the upper atmosphere.

[59] Figure 10 shows the typical photoelectron pattern (plotted separately from the secondary electron fluxes) that comes from studies by *Khazanov et al.* [2011] and takes into account ionosphere-plasmasphere SE transport. This
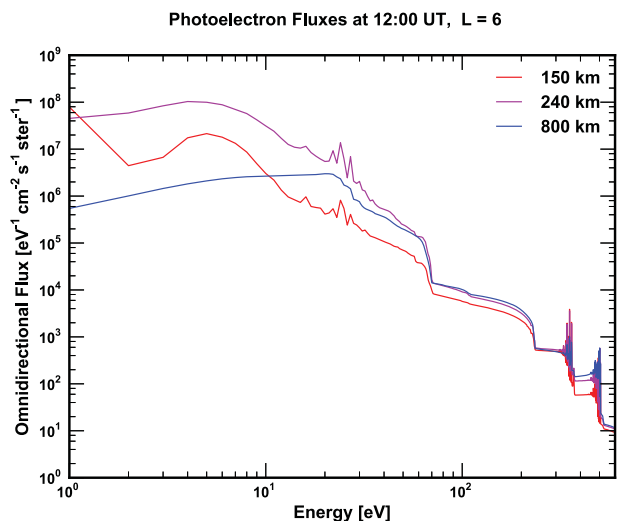
Figure 10. Typical photoelectron pattern in the northern ionosphere, without secondary fluxes, for conditions of symmetric sunlight in both ionospheres at 12:00 UT at altitudes of 150 km (red), 240 km (purple), and 800 km (blue).
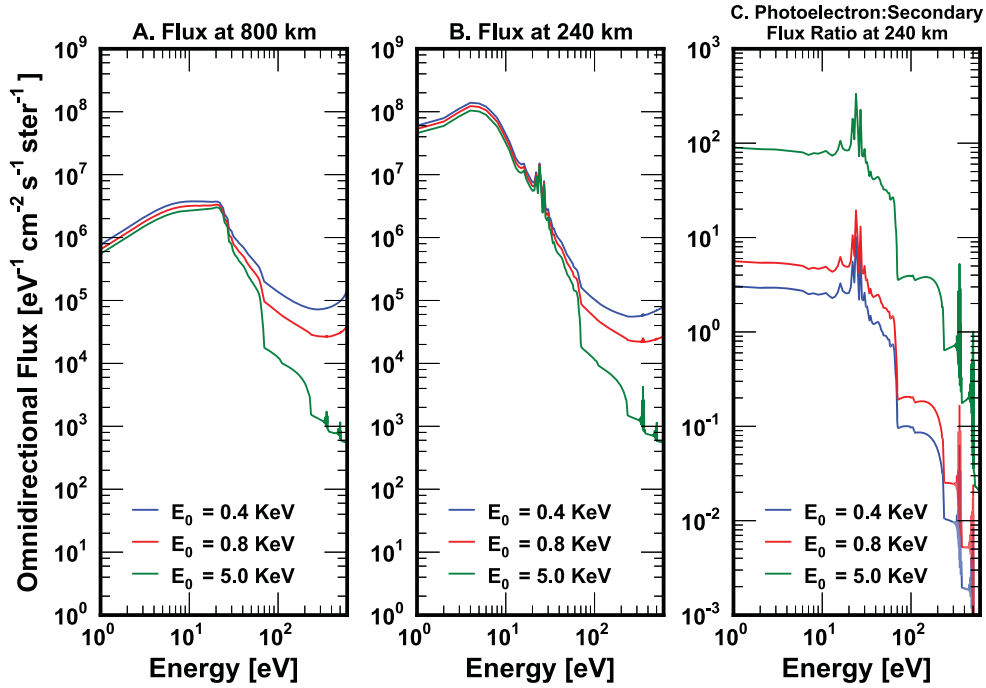
Figure 11. (a) Omnidirectional modeled secondary fluxes ($E < 600$ eV) for the dayside northern iono-sphere at 800 km, including the SE sources of photoionization, secondary production from photoelectron sources, and secondary production from a primary distribution. (b) Omnidirectional dayside secondary fluxes at 240 km. (c) Ratio at 240 km of photoelectron fluxes to secondary electrons form a precipi-tated primary beam. All secondary fluxes from primary precipitation are calculated at 12:00 UT with a total precipitating energy flux 1 erg cm^{-2} s^{-1} and mean energy 0.4 keV (blue), 0.8 keV (red), and 5.0 keV (green).

simulation has been performed under conditions of sym-metric illumination, when both ionospheric foot points are sunlit, at 12:00 UT with $L = 6$. The curves plotted on this figure correspond to the altitudes of 150 km (red), 240 km (purple), and 800 km (blue) in the northern ionosphere, over the energy range 1–600 eV.

[60] The photoelectron spectra presented in the Figure 10 show distinctive characteristics that are the hallmarks of the Earth's photoelectron spectra. The trough feature at the low altitudes (150 km) between 2 and 3 eV comes from losses of photoelectrons in the excitation of N_2 vibrational levels. The spikes between 20 and 30 eV come from photoionization of O and N_2 by the strong 30.4 nm (40.8 eV) irradiance, while the knee near 60 eV comes from a sharp drop in solar irra-diance below 16 nm (75 eV). The sharp rise in flux near the energies of 350 eV and 500 eV comes from Auger ionization by solar irradiance between 1.5 and 3 nm.

[61] The relationship between SE produced by secondary production from photoelectron sources and SE produced by secondary production from primary precipitation is demonstrated in Figure 11. Figures 11a and 11b show mod-eled omnidirectional fluxes in the northern ionosphere at 12:00 UT, which include contributions from each type of dayside SE source: photoionization, secondary produc-tion from photoelectrons, and secondary production from primary precipitation, the latter chosen for a Maxwellian primary beam with total precipitating energy flux of 1

erg cm^{-2} s^{-1} to be comparable with photoelectron fluxes. These secondary fluxes are displayed at two altitudes, 800 km (Figure 11a) and 240 km (Figure 11b), for three pri-mary distribution mean energies: 0.4 keV (blue), 0.8 keV (red), and 5.0 keV (green). The trough observed between 2 and 3 eV at 240 km for secondary fluxes at mid-night, caused by the excitation of N_2 vibrational levels, as explained above in the description of Figure 2, is no longer seen, because with the increased thermal electron density present at 12:00 UT, Coulomb collisional processes become more dominant.

[62] In Figures 11a and 11b, more photoelectron features are visible as the mean energy of the primary precipitation increases. This is because the relative flux contribution of secondary production from photoelectron sources increases as the mean energy of primary precipitation increases, which causes secondary fluxes to decrease in intensity, as seen in Figures 4a and 4b. Thus, for the energy range from 0 to 600 eV, as the mean energy of the primary precipitation increases, photoelectrons dominate more clearly over sec-ondary production from the primary beam, especially for $E > 50$ eV. Figure 11c displays the ratio at 240 km of photoelectron fluxes to secondary electrons from a precip-itated primary beam. This panel shows the increasing rela-tive intensity of photoelectron to secondary electron fluxes as mean energy of the precipitating electron distribution increases, as seen in Figures 11a and 11b.

5. Summary and Conclusion

[63] Diffuse auroral precipitation covers a broad range of geomagnetic latitudes, which map along field lines from the inner magnetosphere to the plasma sheet. Diffuse precipitation of energetic electrons from the magnetosphere is a consequence of pitch angle scattering by different kinds of plasma waves. The precipitation of energetic electrons in the diffuse auroral region is an important source of ionizing energy input to the middle atmosphere and heating of the thermal plasma. The dissipation process of magnetospheric electrons in the diffuse aurora is also affiliated with the cascading of higher-energy electrons toward thermal energies and the production of secondary electrons. This lower energy electron population can escape back to the magnetosphere and become trapped on closed magnetic field lines. In this paper, for the first time, we discussed magnetosphere-ionosphere-atmosphere coupling collisional processes in the electron diffuse aurora, focusing on the energy and particle interplay between the two magnetically conjugate ionospheres and outer plasmasphere.

[64] We found quantitative relations between the energy and particle fluxes that precipitate from the magnetosphere into the ionosphere and the affiliated secondary electron population escaping back to the magnetosphere (Figures 4–7). The SEs that travel to the magnetosphere can be trapped by the Earth's magnetic field and deliver a portion of their energy to the thermal electrons of the outer plasmasphere (Figure 7). This energy, however, does not stay in the magnetosphere, because thermal conductivity is the fastest process of the energy loss in the plasmasphere and all of the energy that was collected along the field tube will flow down to the ionosphere, contributing to the ionospheric energy balance between thermal electrons and ions.

[65] As we have demonstrated, there is a very complicated energy interplay between the two magnetically conjugated ionospheres and the outer plasmasphere. Our quantitative analysis has been made in order to address this issue by studying different limited cases when one of the conjugated ionospheres was completely or partially separated from such energy, an exchange between the plasmasphere and another ionosphere (Figures 5–7). We have also seen that the mean energy of the precipitating diffuse auroral electrons has a significant effect on the relative role of secondary flux intensity, cascading (Figure 8), and photoelectron production on the dayside (Figure 11).

[66] As we pointed out in the introduction to our paper, the diffuse aurora, which is always present and widely distributed in rings around Earth's magnetic poles, collectively accounts for about three-quarters of the auroral energy precipitating into the ionosphere [e.g., *Newell et al.*, 2009]. For this reason, as demonstrated by the quantitative analysis presented in this paper, diffuse auroral precipitation must be included in the development of global models by taking into account ionosphere-magnetosphere energy interplay between precipitated high-energy electrons of magnetospheric origin, the resultant secondary electron population escaping back to the magnetosphere, its trapping in this region, and its heating of the thermal population of the outer plasmasphere, with the consequent thermal conductivity flux formation that returns back to the upper ionosphere. Neglecting any of these processes will yield an incomplete picture.

References

Arnoldy, R. L., P. O. Isaacson, and P. B. Lewis (1974), Field-aligned auroral electron fluxes, *J. Geophys. Res.*, *79*, 4208–4221, doi:10.1029/JA079i028p04208.

Banks, P. M., C. R. Chappell, and A. F. Nagy (1974), A new model for the interaction of auroral electrons with the atmosphere: Spectral degradation, backscatter, optical emission, and ionization, *J. Geophys. Res.*, *79*, 1459–1470, doi:10.1029/JA079i010p01459.

Bell, K. L., and R. P. Stafford (1992), Photoionization cross-sections for atomic oxygen, *Planet. Space Sci.*, *40*, 1419–1424, doi:10.1016/0032-0633(92)90097-8.

Bilitza, D. (1990), Progress report on IRI status, *Adv. Space Res.*, *10*, 3–5, doi:10.1016/0273-1177(90)90298-E.

Conway, R. (1988), *Photoabsorption and Photoionization Cross Sections: A Compilation of Recent Measurements*, NRL Memo Rep. 6155, Naval Research Laboratory, Washington, D. C.

Eather, R. H., and S. B. Mende (1971), Airborne observations of auroral precipitation patterns, *J. Geophys. Res.*, *76*, 1746–1755, doi:10.1029/JA076i007p01746.

Ebihara, Y., T. Sakanoi, K. Asamura, M. Hirahara, and M. F. Thomsen (2010), Reimei observation of highly structured auroras caused by nonaccelerated electrons, *J. Geophys. Res.*, *115*, A08320, doi:10.1029/2009JA015009.

Evans, D. S. (1974), Precipitating electron fluxes formed by a magnetic field aligned potential difference, *J. Geophys. Res.*, *79*, 2853–2858, doi:10.1029/JA079i019p02853.

Fennelly, J. A., and D. G. Torr (1992), Photoionization and Photoabsorption Cross Sections of O, N_2 O_2, and N for Aeronomic Calculations, *Atom. Data Nucl. Data Tables*, *51*, 321, doi:10.1016/0092-640X(92)90004-2.

Fontaine, D., and M. Blanc (1983), A theoretical approach to the morphology and the dynamics of diffuse auroral zones, *J. Geophys. Res.*, *88*, 7171–7184, doi:10.1029/JA088iA09p07171.

Frank, L. A., and K. L. Ackerson (1971), Observations of charged particle precipitation into the auroral zone, *J. Geophys. Res.*, *76*, 3612–3643, doi:10.1029/JA076i016p03612.

Hardy, D., M. Gussenhoven, R. Raistrick, and W. McNeil (1987), Statistical and fuctional representation of the pattern of auroral energy flux, number flux, and conductivity, *J. Geophys. Res.*, *92*, 12,275–12,294.

Hedin, A. (1991), Extension of the MSIS thermosphere model into the middle and lower atmosphere, *J. Geophys. Res.*, *96*, 1159–1172.

Hinteregger, H., K. Fukui, and B. Gibson (1981), Observational, reference and model data on solar EUV from measurements on AE-E, *Geophys. Res. Lett.*, *8*, 1147–1150.

Hoffman, R. A., and J. L. Burch (1973), Electron precipitation patterns and substorm morphology, *J. Geophys. Res.*, *78*, 2867–2884, doi:10.1029/JA078i016p02867.

Johnstone, A. D., D. M. Walton, R. Liu, and D. A. Hardy (1993), Pitch angle diffusion of low-energy electrons by whistler mode waves, *J. Geophys. Res.*, *98*, 5959–5967, doi:10.1029/92JA02376.

Kennel, C. F., and H. E. Petschek (1966), Limit on stably trapped particle fluxes, *J. Geophys. Res.*, *71*, 1–28.

Khazanov, G. (1979), The Kinetics of the Electron Plasma Component of the Upper Atmosphere, Nauka, Moscow, [English translation: #80-50707, National Translation Center, Washington, D. C. 1980].

Khazanov, G. (2011), *Kinetic Theory of the Inner Magnetospheric Plasma*, Astrophysics and Space Science Library, Springer.

Khazanov, G., M. W. Liemohn, T. I. Gombosi, and A. F. Nagy (1993), Non-steady-state transport of superthermal electrons in the plasmasphere, *Geophys. Res. Lett.*, *20*, 2821–2824.

Khazanov, G. V., M. A. Koen, I. V. Konikov, and I. M. Sidorov (1984), Simulation of ionosphere-plasmasphere coupling taking into account ion inertia and temperature anisotropy, *Planet. Space Sci.*, *32*, 585–598, doi:10.1016/0032-0633(84)90108-9.

Khazanov, G. V., T. Neubert, and G. D. Gefan (1994), Unified theory of ionosphere-plasmasphere transport of suprathermal electrons, *IEEE T. Plasma Sci.*, *22*, 187–198, doi:10.1109/27.279022.

Khazanov, G. V., M. W. Liemohn, T. S. Newman, M.-C. Fok, and R. W. Spiro (2003), Self-consistent magnetosphere-ionosphere coupling: Theoretical studies, *J. Geophys. Res.*, *108*, 1122, doi:10.1029/2002JA009624.

Khazanov, G. V., D. E. Rowland, T. E. Moore, and M. R. Collier (2011), The VISIONS Science, Abstract SM31A-2087 presented at 2011 Fall Meeting, AGU, San Francisco, Calif.

Khazanov, G. V., A. Glocer, M. W. Liemohn, and E. W. Himwich (2013), Superthermal electron energy interchange in the ionosphere-plasmasphere system, *J. Geophys. Res. Space Physics*, *118*, 925–934, doi:10.1002/jgra.50127.

Link, R. (1992), Feautrier solution of the electron transport equation, *J. Geophys. Res.*, *97*, 159–169, doi:10.1029/91JA02214.

Lui, A. T. Y., and C. D. Anger (1973), A uniform belt of diffuse auroral emission seen by the ISIS-2 scanning photometer, *Planet. Space Sci.*, *21*, 799–799, doi:10.1016/0032-0633(73)90097-4.

Lui, A. T. Y., S.-I. Akasofu, D. Venkatesan, C. D. Anger, W. J. Heikkila, J. D. Winningham, and J. R. Burrows (1977), Simultaneous observations of particle precipitations and auroral emissions by the Isis 2 satellite in the 19-24 MLT sector, *J. Geophys. Res.*, *82*, 2210–2226, doi:10.1029/JA082i016p02210.

Lummerzheim, D., and J. Lilensten (1994), Electron transport and energy degradation in the ionosphere: Evaluation of the numerical solution, comparison with laboratory experiments and auroral observations, *Ann. Geophys.*, *12*, 1039–1051, doi:10.1007/s00585-994-1039-7.

Lyons, L. R. (1974), Pitch angle and energy diffusion coefficients from resonant interactions with ion-cyclotron and whistler waves, *J. Plasma Phys.*, *12*, 417–432, doi:10.1017/S002237780002537X.

Meng, C.-I., B. Mauk, and C. E. McIlwain (1979), Electron precipitation of evening diffuse aurora and its conjugate electron fluxes near the magnetospheric equator, *J. Geophys. Res.*, *84*, 2545–2558, doi:10.1029/JA084i06p02545.

Min, Q.-L., D. Lummerzheim, M. H. Rees, and K. Stamnes (1993), Effects of a parallel electric field and the geomagnetic field in the topside ionosphere on auroral and photoelectron energy distributions, *J. Geophys. Res.*, *98*, 19,223–19,234, doi:10.1029/93JA01742.

Mishin, E. V., A. A. Trukhan, and G. V. Khazanov (1990), Plasma effects of superthermal electrons in the ionosphere, Nauka, Moscow.

Newell, P. T., T. Sotirelis, and S. Wing (2009), Diffuse, monoenergetic, and broadband aurora: The global precipitation budget, *J. Geophys. Res.*, *114*, A09207, doi:10.1029/2009JA014326.

Newell, P. T., A. R. Lee, K. Liou, S.-I. Ohtani, T. Sotirelis, and S. Wing (2010), Substorm cycle dependence of various types of aurora, *J. Geophys. Res.*, *115*, A09226, doi:10.1029/2010JA015331.

Nishimura, Y., et al. (2013), Structures of dayside whistler-mode waves deduced from conjugate diffuse aurora, *J. Geophys. Res. Space Physics*, *118*, 664–673, doi:10.1029/2012JA018242.

Peticolas, L., and D. Lummerzheim (2000), Time-dependent transport of field-aligned bursts of electrons in flickering aurora, *J. Geophys. Res.*, *105*, 12,895–12,906, doi:10.1029/1999JA000398.

Rees, D. (1989), *Physics and Chemistry of the Upper Atmosphere*, Cambridge Univ. Press, New York, NY.

Schumaker, T. L., R. L. Carovillano, M. S. Gussenhoven, and D. A. Hardy (1989), The relationship between diffuse auroral and plasma sheet electron distributions near local midnight, *J. Geophys. Res.*, *94*, 10,061–10,078, doi:10.1029/JA094iA08p10061.

Solomon, S., P. Hays, and V. Abreu (1988), The auroral 6300Å emission: Observations and modeling, *J. Geophys. Res.*, *93*, 9867–9882.

Solomon, S. C. (1993), Auroral electron transport using the Monte Carlo method, *Geophys. Res. Lett.*, *20*, 185–188, doi:10.1029/93GL00081.

Stamnes, K. (1981), On the two-stream approach to electron transport and thermalization, *J. Geophys. Res.*, *86*, 2405–2410, doi:10.1029/JA086iA04p02405.

Strickland, D. J., D. L. Book, T. P. Coffey, and J. A. Fedder (1976), Transport equation techniques for the deposition of auroral electrons, *J. Geophys. Res.*, *81*, 2755–2764, doi:10.1029/JA081i016p02755.

Winningham, J. D., W. J. Heikkila, F. Yasuhara, and S.-I. Akasofu (1975), The latitudinal morphology of 10-eV to 10-keV electron fluxes during magnetically quiet and disturbed times in the 2100-0300 MLT sector, *J. Geophys. Res.*, *80*, 3148–3171, doi:10.1029/JA080i022p03148.